Surfaces and Interfaces 48 (2024) 104143

Contents lists available at ScienceDirect

Surfaces and Interfaces

journal homepage: www.sciencedirect.com/journal/surfaces-and-interfaces

Enhanced hydrogen peroxide production and organic substrates degradation using atomically dispersed antimony P-doped carbon nitride photocatalysts

Elisa Gaggero [a], Wenan Cai [b], Paola Calza [a,*], Teruhisa Ohno [b]

[a] Department of Chemistry, University of Turin, Via Pietro Giuria 5, Turin 10126, Italy
[b] Department of Applied Chemistry, Faculty of Engineering, Kyushu Institute of Technology, 1-1 Sensuicho, Tobata, Kitakyushu, Japan

ARTICLE INFO

Keywords:
Carbon nitride
Hydrogen peroxide production
Organic pollutants degradation
Phosphorus doping
Atomically dispersed antimony

ABSTRACT

In this work atomically dispersed antimony P-doped carbon nitride was prepared with the aim of producing hydrogen peroxide under visible light irradiation and of obtaining organic contaminants degradation. The conjugation of the P-doping can induce significant increase in visible light harvesting, narrowing of band gap energy and shift of the upper edge of the VB to less positive value and the introduction of Sb can efficiently trap oxygen molecules in the Sb-OO end-on structure and at the same time accumulate electrons which act as the photoreduction sites for O_2 via a $2e^-$ ORR pathway. Pristine C_3N_4 and P-doped C_3N_4 were prepared as references using melamine and ammonium dihydrogen phosphate as precursors and different amount of Sb were added (x = 0.5, 1, 3, 5 mmol) to synthetize Sbx P-doped C_3N_4. All materials were characterized with multiple techniques, tested for the hydrogen peroxide production and for the degradation of carbamazepine. The pristine C_3N_4 led to a H_2O_2 poor production but with the introduced modifications the yield increased and an upward trend during the time was observed. The optimum amount of Sb was found to be 1 mmol and it led to the production of more than 7 times the amount produced by pristine carbon nitride. The degradation of carbamazepine using only visible radiation required prolonged timescales but when we expand the light spectrum to include near-UV, the abatement of the pollutant is achieved in a few hours. The efficiency of the synthesized materials in hydrogen peroxide production suggests possible future developments that take advantage of the excellent peroxide production of atomically dispersed antimony P-doped carbon nitride photocatalysts in Fenton-like processes or involve the use of peroxidase enzymes to achieve enhanced degradative performances.

1. Introduction

The scarcity of water and the worsening of its quality due to pollution is one of the great crises that the modern world is facing. Traditional water treatment plants are often unable to remove contaminants of emerging concern, and the development of new methodologies that are effective in removing these pollutants while being environmentally friendly and low cost is of paramount importance [1,2]. Photocatalysis and the use of reactive oxygen species (ROS) are viable strategies for the removal of organic contaminants, and research in this field is focusing on modifying and doping photocatalysts to increase their degradative performance and to be able to use sunlight efficiently [3–5].

Hydrogen peroxide is extensively used for the activation of hydroxyl radicals (·OH) for wastewater treatment by exploiting Fenton or Fenton-like processes, due to its high oxygen content and the absence of harmful by-products [6–8]. Moreover, H_2O_2 is necessary to activate peroxidase, an enzyme widely distributed in nature, which can be easily extracted from plant cells and some animal tissues and organs [9]. Because of its properties, such as low selectivity and high resistance to chemical and thermal denaturation, this enzyme appears to be suitable for biotechnological applications, such as the removal of phenol and phenolic derivatives or the degradation of dyes [10–12].

The traditional industrial process for H_2O_2 production (over 95 % of total production) is the anthraquinone oxidation process that includes hydrogenation and oxidation reactions that consume significant amounts of energy and generates a lot of waste resulting in a not environmentally sustainable process [13,14]. Therefore, recently, large attention has been directed to the possibility of efficiently producing

* Corresponding author.
E-mail address: paola.calza@unitot.it (P. Calza).

https://doi.org/10.1016/j.surfin.2024.104143
Received 31 October 2023; Received in revised form 16 February 2024; Accepted 3 March 2024
Available online 4 March 2024

H_2O_2 by a photocatalytic reaction process, particularly through carbon nitride-based materials [15,16]. However, the activity of pristine g-C_3N_4 is still restricted by low efficiency because of high rate of charge recombination due to defects introduced into the structure following polymerization, large band gap (2.7 eV) and small absorption of visible light which results in inadequate visible-light harvesting [17–19]; moreover, to achieve high efficiency for H_2O_2 production, it is crucial to boost the $2e^-$ oxygen reduction reaction (ORR, Eq. (1)) or the $2e^-$ water oxidation reaction (WOR, Eq. (3)) whereas when using pristine carbon nitride, it is difficult to prevent the competitive stepwise $1e^-$ to $1e^-$ ORR [20].

$$O_2+2H^++2e^-\leftrightarrow H_2O_2 \text{ (0.695V vs. NHE)} \quad (1)$$

$$2H_2O+4\,h^+\leftrightarrow O_2+4H^+ \text{ (1.23V vs. NHE)} \quad (2)$$

$$H_2O_2 + 2H^+ + 2e^- \leftrightarrow 2H_2O \text{ (1.76V vs. NHE)} \quad (3)$$

With the aim of addressing these issues, several strategies have been studied such as metal [21–24] and non-metal doping [25,26]. In this work atomically dispersed antimony P-doped carbon nitride was prepared. In fact, according to the literature the P-doping can induce significant increase in visible light harvesting, narrowing of band gap energy, shift of the upper edge of the VB to less positive value and the decrease of binding energy between electrons and holes [27–30]; additionally, it can boost charge transfer mobility since the lone electron that is still present can delocalize from the P atom to the p-conjugated triazine ring, resulting in the induction of an electron-rich state [31,32]. On the other hand, the introduction of single Sb sites that can accumulate electrons, which act as photoreduction sites for O_2 via a $2e^-$ ORR pathway [33] and is expected to provide effective photogenerated carrier charge transfer, lower carrier recombination rates, therefore raising the efficiency of photocatalytic hydrogen production [34].

Pristine C_3N_4 and P-doped C_3N_4 were prepared as references using melamine and ammonium dihydrogen phosphate as precursors and different amount of Sb were added (x = 0.5,1,3,5 mmol) to synthetize Sbx P-doped C_3N_4. All materials were characterized with multiple instrumental techniques (x-ray diffraction, photoluminescence, X-ray photoelectron spectroscopy, UV–visible spectroscopy, FT-IR and electrochemical analysis). Prepared photocatalysts were then tested for hydrogen peroxide production without using a sacrificial reagent exploiting visible light and for the degradation of a model pollutant, namely carbamazepine (CBZ). This was chosen since it is a common anticonvulsant primarily used to treat epilepsy and nerve pain currently consumed in large quantities worldwide and after its oral administration, only 72 % is absorbed by the human body and metabolized up to a 99 % level, while the rest is discharged into the sewage system where is scarcely degraded [35–37].

2. Experimental

Ammonium dihydrogen phosphate, carbamazepine (>99 %), melamine (99 %), sodium hexafluoroantimonate (V), thiourea (99 %), 4-aminoantipyrin, phenol, phosphoric acid (≥85.0 %), acetonitrile and ethanol were purchased by Sigma Aldrich. All solutions were prepared with ultrapure water Millipore Milli-Q™ (TOC < 2 ppb, conductivity≥18MΩ cm).

2.1. Synthesis of the photocatalysts

The synthesis of pristine C_3N_4 was performed through the following procedure: melamine (10 g) was heated in N_2 atmosphere in a closed ceramic crucible up to 520 °C at 3 °C min^{-1}, the temperature was maintained for 2 h and then it was cooled down obtaining bulk graphitic carbon nitride. Phosphorous doped C_3N_4 material was prepared by adding slowly 2 g of $NH_4(H_2PO_4)$ to an aqueous suspension containing melamine (10 g). The final suspension was stirred at room temperature for 1 h and then heated at 50 °C until complete dryness. The obtained powder (A) was calcinated with the same temperature programme described above and the resulting material was labelled P-doped C_3N_4 [27]. Sb(x) P-doped C_3N_4 materials, where x indicates Sb mmols, were prepared by wet chemical method synthesis. X mmol of $NaSbF_6$ were dissolved in 120 mL of EtOH (x = 0,0.5, 1, 5, 15) and the flask was kept in an ultrasound bath for 60 min at 60 °C. Then, 4 g of (A) were added and maintained in ultrasound bath for 60 min at 60 °C. The solvent in the solution was removed by rotatory evaporation and the obtained white powder was transferred into a tube furnace and calcinated increasing the temperature to 560 °C at a ramp rate of 2 °C min^{-1} in N_2 atmosphere then keeping it at 560 °C for 4 h [33].

2.2. Characterization

The crystalline phases of the synthetized photocatalysts were characterized by a powder X–ray diffraction (XRD) instrument (MiniFlex II, Rigaku Co.) with CuKα (λ=1.5418 Å) radiation (cathode voltage: 30 kV, current: 15 mA). Fourier transform infrared spectra were recorded with an FT-IR spectrometer (IR Shimadzu Prestige-21). X–ray photoelectron spectroscopy (XPS) measurements were performed using a Kratos AXIS Nova spectrometer (Shimadzu Co.) with a monochromatic Al Kα X-ray source. UV–vis diffuse reflectance spectroscopy (UV-DRS) was executed using a UV/VIS/NIR spectrometer UV-2600 (Shimadzu Co.). Photoluminescence (PL) spectroscopy was acquired using a FP-8500 spectrofluorometer (JASCO Corporation, Japan). An electrochemical workstation CHI760E (Chenhua corporation) was used to test the Mott-Schottky plots. Morphological analyses were performed with FEG-SEM TESCAN model S9000G, Schottky-type FEG source, theoretical resolution in In-Beam SE (Ultra High Resolution) mode: 0.7 nm at 15 keV. Point microanalysis and element distribution maps were obtained with energy dispersive spectrometer (EDS) for X-ray microanalysis, OXFORD EDS Ultim Max detector and AZTEC Software. The samples were deposited on special aluminium stubs to which double-sided carbon tape was applied in advance to facilitate conductivity and subsequently samples were subjected to metallization with a thin layer of chromium (5 nm).

Branauer-Emmett-Teller (BET) surface area measurements were performed by a full analysis of nitrogen adsorption-desorption tests at liquid nitrogen temperature of 77 K.

Electron Paramagnetic Resonance (EPR) spectroscopy using an Adani EPR, working in CW, X bad. The samples have been prepared according to the following procedures: 10 mg of samples in 0,5 ml 0,044 M DMPO. The formation of OH radicals has been evaluated for the samples under irradiation with a light > 420 nm.

2.3. Hydrogen peroxide production

All the synthetized photocatalysts were tested for the hydrogen peroxide production, using a concentration equal to 2 g/L. No sacrificial reagent was used, so Milli-Q water was used as reaction medium, and oxygen was bubbled for 15 min before starting to irradiate with a Xenon lamp equipped with cut off filters so that the range of wavelengths used to irradiate could be modulated; specifically, a filter was used to cut wavelengths below 420 nm to simulate visible light and a filter at 340 nm to also include near UV-A and simulate sunlight. The concentration of produced hydrogen peroxide was determined at three sampling time for five hours and was determined by a colorimetric method using PACKTEST (WAK-H2O2, Kyoritsu Chemical-Check Laboratory, Corp.) equipped with a digital PACKTEST spectrometer (ED723, GL Sciences Inc.) or by using the horseradish peroxidase-coupled oxidations method described by Frew et al. [38]. Experiments were repeated using ultrapure water as reaction medium without oxygen bubbling prior to irradiation. Analyses of Na content in the samples after irradiation was carried out with an inductively coupled plasma optical emission spectrometer (ICP-OES), the Perkin Elmer Optima 7000 (Perkin Elmer,

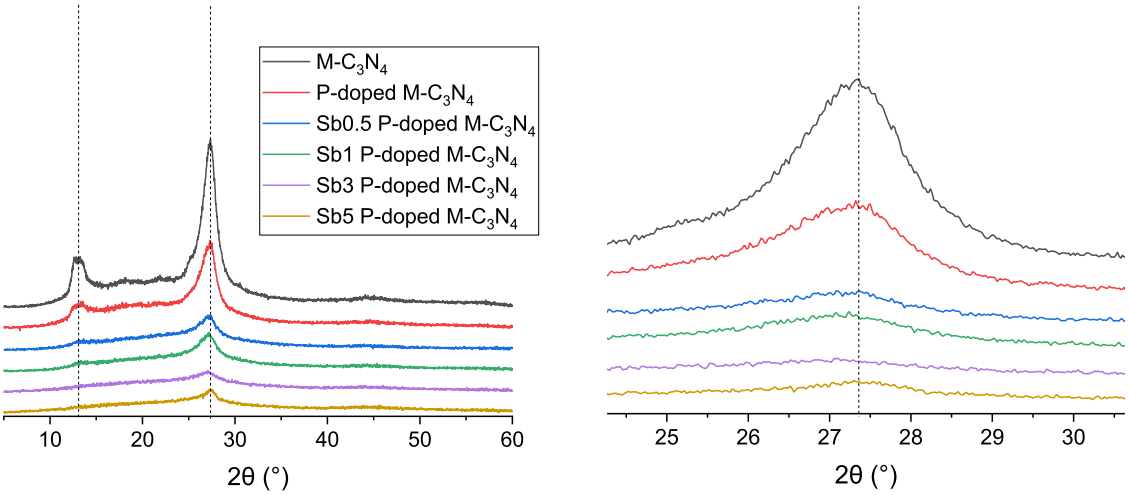

Fig. 1. XRD patterns of prepared samples and enlargement of the region between 25° and 30°

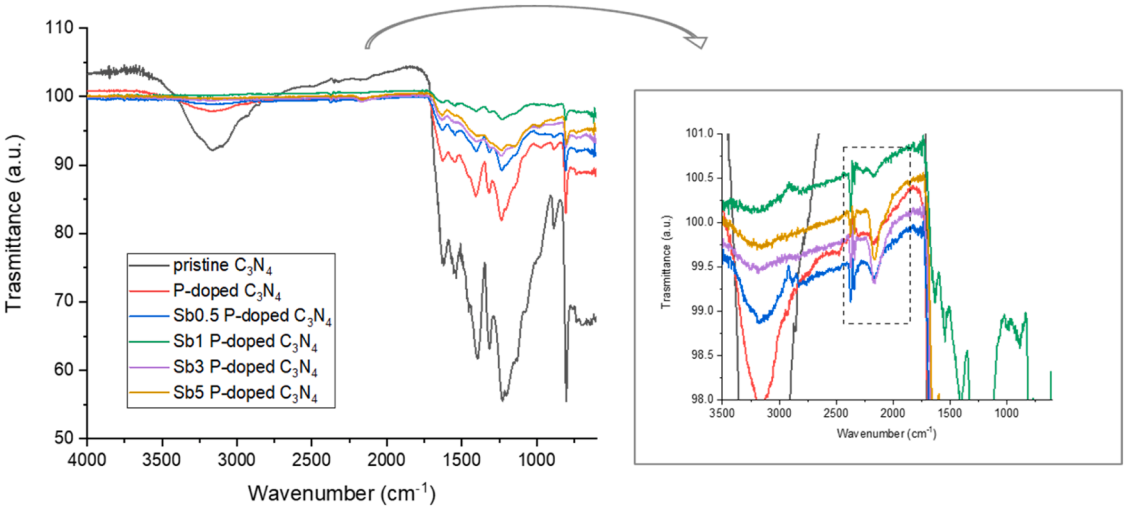

Fig. 2. FTIR spectra of the synthetized photocatalysts.

Norwalk, CT, USA).

2.4. Organic substrates degradation

The degradation tests were performed on a solution of carbamazepine at 10 mg/L at natural pH (pH = 7.1) in the presence of the photocatalyst at 0.5 g/L. Experiments were carried on in Pyrex glass cells kept under magnetic stirring and filled with 5 mL of sample and catalyst suspension. The cells were irradiated in a Solarbox (CO.FO.MEGRA Milan, Italy) equipped with a 340 or 420 nm cut-off filter. The samples were filtered through a 0.45 μm PTFE membrane and the photodegradation process was followed over time. Analyses were performed with a Merck-Hitachi HPLC system equipped with a L-6200A Intelligent Pump, a L-4200 UV–VIS Detector and a six-way Rheodyne valve injection system. The detection wavelength was set at 285 nm eluting with 65 % of phosphoric acid solution at pH 2.8 and 35 % of acetonitrile at a flow rate of 1 mL/min. The retention time was 5.1 min.

Adsorption tests were performed keeping the samples containing carbamazepine and photocatalysts in the dark for sixteen hours. Moreover, in order to further comprehend the mechanism of degradation of carbamazepine by synthetized photocatalysts, experiments were repeated using EtOH as holes' scavenger.

3. Results and discussion

3.1. Morphology and structural information

XRD measurements were used to initially explore the crystalline structures of synthetized materials (Fig. 1). XRD patterns of all samples revealed two characterisation peaks at about 27.3° and 13.2°, related to the interlayer stacking (002) and the inner planar structure packing (100) of tri-s-triazine units, respectively [39]. They reveal the presence of graphitic C_3N_4 phase only for pristine and modified samples, showing that the precursors are entirely condensed, and no crystalline phosphate impurities are present. The intensity of the diffraction maxima measured in Sb(x) P-doped materials is lower than in pristine sample and it decreases especially with samples with a higher amount of antimony. The considerable decrease in peak intensity at 13.2°, corresponding to the (100) plane, indicates a lower crystallinity degree than the pristine material. The position of the peak at 27.3° attributed to the (002) plane undergoes a little shift because of the electrostatic repulsion between interlayers matrix caused by the positive ions incorporated into the matrix.

The FTIR spectra of all the photocatalysts are displayed in Fig. 2 and confirmed the carbon nitride structure of the materials, no major changes between the samples are revealed. The broad groups of peaks

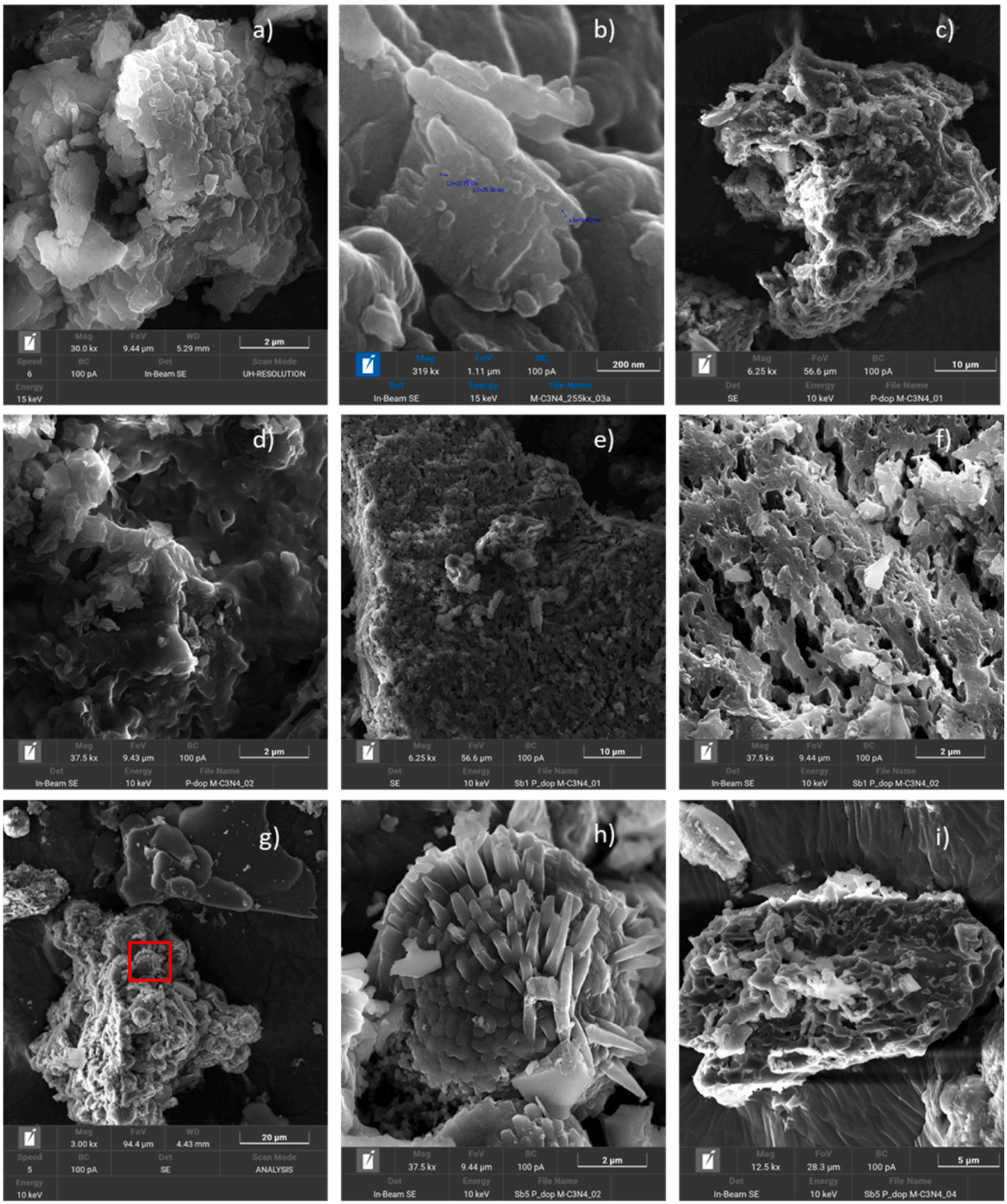

Fig. 3. FEG-SEM images of a) pristine C_3N_4 2 µm, b) pristine C_3N_4 200 nm, c) P-doped C_3N_4 10 µm, d) P-doped C_3N_4 2 µm, e) Sb1 P-doped C_3N_4 10 µm, f) Sb1 P-doped C_3N_4 1 µm, g) Sb5 P-doped C_3N_4 20 µm, h) Sb5 P-doped C_3N_4 2 µm (enlargement of the red square of g), i) Sb5 P-doped C_3N_4 5 µm.

extending from 3500 to 2700 cm^{-1} are attributed to O—H and N—H stretching bands because of the presence of adsorbed water and uncondensed amino groups on the surface.

The strong absorption bands in the 1650–1000 cm^{-1} region are typical C=N and C—N stretching vibrations modes of heptazine heterocyclic ring units. The absorptions at 810 cm^{-1} correspond to the tris-triazine breathing mode [27]. FTIR spectra of Sb(x) P-doped C_3N_4 look very similar to that of pristine carbon nitride, except for the signal

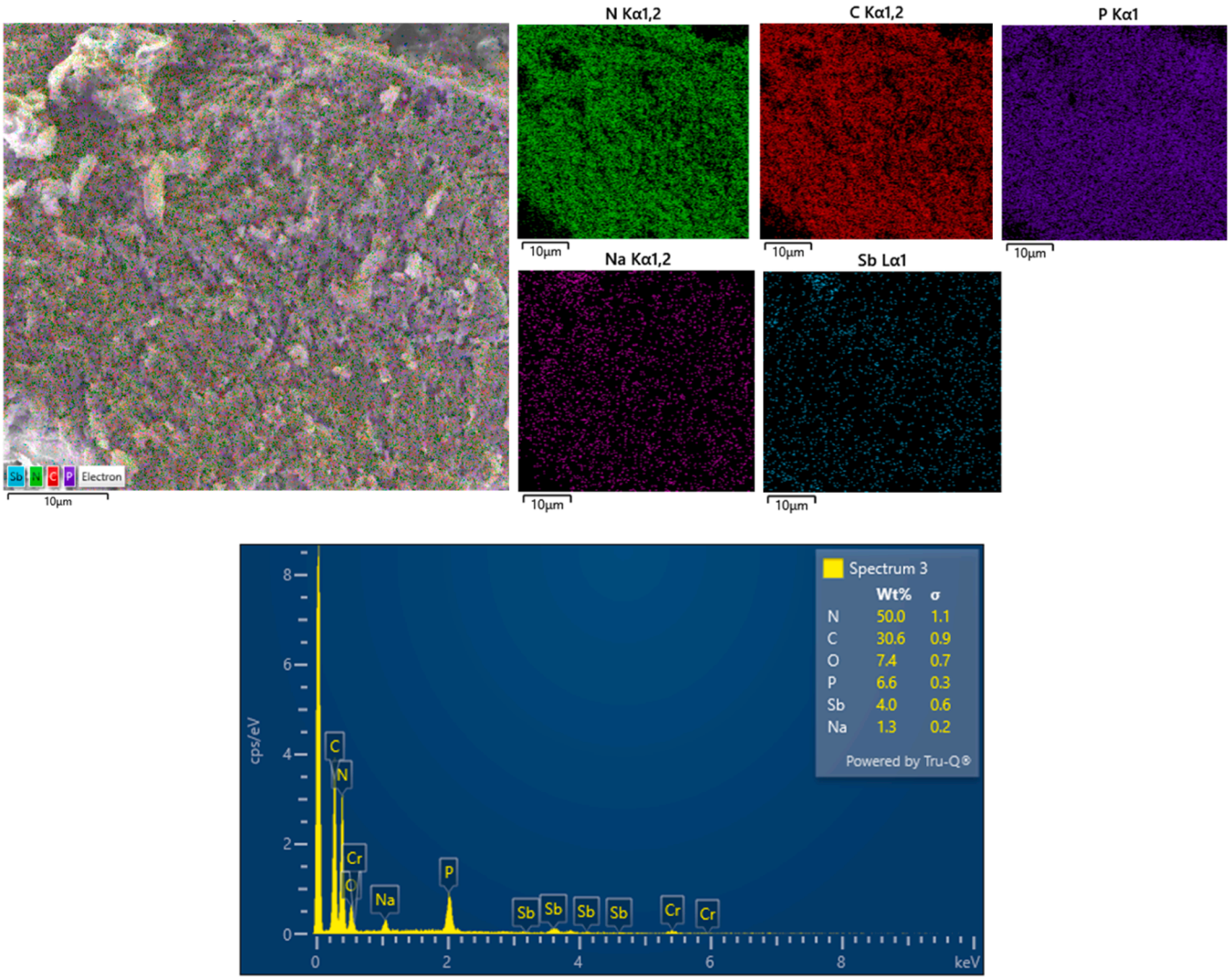

Fig. 4. EDS map and elemental spectrum of Sb1 P-doped C_3N_4.

around 2167 cm^{-1} that is due to the introduction of antimony, and it is related to –C≡N- [40], demonstrating that their chemical structures are essentially consistent. The existence of phosphate cannot be established by *P=O* stretching, which is in the same range as heptazine stretching modes. Moreover, no additional vibrational group can be observed after functionalizing with Sb.

To investigate the morphology of the samples, analyses were performed with a FEG-SEM and the obtained images are shown in Fig. 3.

The average dimension of C_3N_4 particles is around 20 nm and looking at the pure sample in comparison with the phosphorus-doped sample, a slight morphological alteration can be noticed.

On the other hand, the addition of antimony leads to a noticeable alteration in the structure. In fact, the sample becomes more porous and BET analyses show that the surface area is slightly influenced by P and Sb doping ranging from 5 to 6 m^2/g for pristine C_3N_4 and Sb P-doped C_3N_4. Interestingly, in the sample with the highest concentration of antimony (as shown in Fig. 3g and h), distinct morphological regions can be observed within the same sample and upon closer examination, a very distinctive structure appeared, which has been identified as an agglomerate.

Energy Dispersive Spectroscopy (EDS) and Element Mapping Analyses were utilized to provide additional confirmation of the compositions and the spatial distribution of elements in the materials.

As shown in Fig. 4, the EDX results indicate that the main components of the sample are C, N, O P, Sb and Na, the latter deriving from the precursor used for the synthesis of antimony-containing materials, namely $NaSbF_6$. Elemental mapping reveals that N and C elements are the main components and evidences a homogeneous distribution of P and Sb throughout the sample, indicating the successful incorporation of P into the structure of C_3N_4 and the uniform dispersion of antimony throughout the sample.

To further reveal the surface chemical compositions of the obtained materials, X-ray photoelectron spectra (XPS) were recorded, as shown in Fig. 5. The presence of phosphorus as a dopant is also evident from the XPS analysis (Fig. 5e). In fact, the binding energy peak of P 2p in P-doped C_3N_4, centred around 133.4 eV is typical of P-N coordination, indicating the presence of phosphorus incorporated into the C_3N_4 structure with the phosphorus heteroatom that can either replace corner or bay carbons in the structure, forming a P-N bond in the doped C_3N_4, or occupy interstitial positions, forming two P-N bonds [27,41].

The C 1s spectrum (Fig. 5c) of C_3N_4 can be deconvoluted into three peaks, with the main ones located at 284.8 eV and 288.2 eV, respectively. The peak at 284.8 eV can be attributed to carbon impurity signals. The more intense peak with a binding energy of 288.2 eV can be identified as sp^2 hybridized carbon in an aromatic ring containing nitrogen (N—C=N).

The N 1 s spectrum (Fig. 5d) can be deconvoluted into three peaks with binding energies of 398.6 eV, 400.1 eV, and 401.1 eV, respectively.

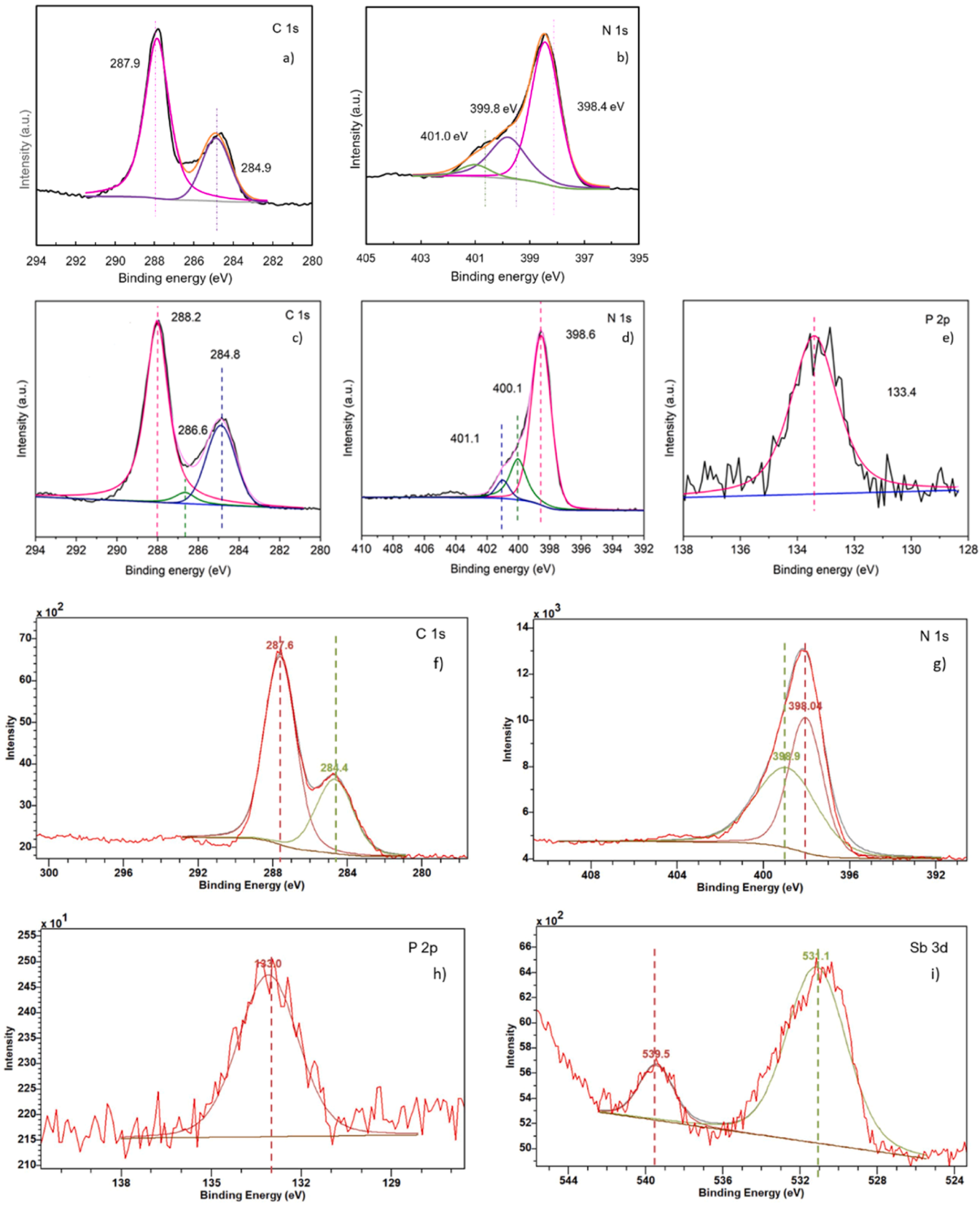

Fig. 5. High-resolution C 1s (a), N 1s (b) XPS spectra C_3N_4 C 1s (c), N 1s (d) and P 2p (e) XPS spectra of P-doped C_3N_4 and C 1s (f), N 1s (g), P 2p (h) and Sb 3d (i) XPS spectra of Sb1 P-doped C_3N_4.

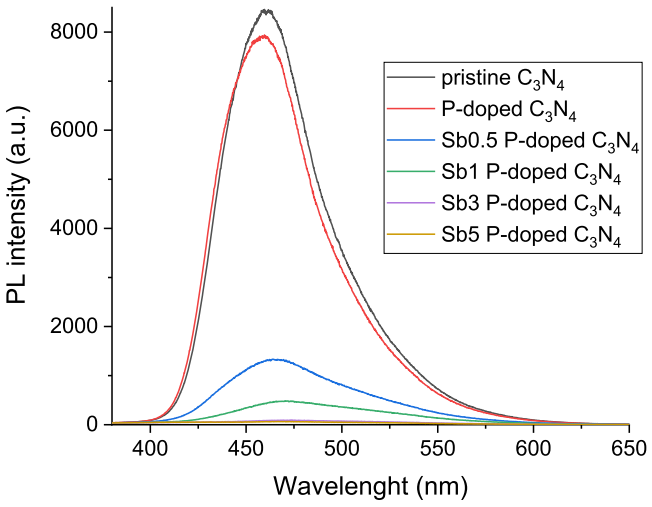

Fig. 6. Photoluminescence spectra for all samples.

The main peak at 398.6 eV is assigned to sp^2 hybridized nitrogen in triazine rings containing C triazine (C—N=C), while the peak at 400.1 eV is typically attributed to tertiary nitrogen groups N-$(C)_3$. The peak at 401.1 eV indicates the presence of amino groups (N—H) [42–44]. Therefore, XPS analyses further confirm the triazine heterocyclic ring structure of the P-doped C_3N_4.

XPS spectroscopy of C 1s of the Sb1 P-doped C_3N_4 material shows no substantial difference from the antimony-free material. The binding energy of Sb 3d, specifically Sb $3d_{3/2}$ at 539.5 eV and Sb $3d_{5/2}$ at 531.1 eV, is close to that of Sb_2O_3 (Sb $3d_{3/2}$ at 539.8 eV and Sb $3d_{5/2}$ at 530.5 eV)[33,45], suggesting that the oxidation state of Sb is close to +3.

3.2. Charge transfer properties

Photoluminescence analyses were employed to investigate charge recombination in synthesized photocatalysts, enhancing our comprehension of their effectiveness and the transport dynamics of charge carriers in different materials. Indeed, this technique yields valuable insights into the behaviour of charge carriers, electrons and holes, by measuring the emission of photons, i.e., luminescence, that occurs when these charge carriers recombine after the material has been exposed to light; therefore, stronger photoluminescence intensity corresponds to a higher charge recombination [46,47].

As shown in Fig. 6, the influence of the amount of antimony on charge recombination is marked; in fact, the intensity of photoluminescence noticeably decreases when increasing the Sb millimoles, so indicating that electron-hole recombination is suppressed. In fact, the intermediate band in the band structure can be eliminated by incorporating atomically dispersed antimony with the d10 electronic configuration. This is advantageous for effective charge separation and the formation of reactive centers with a high density of electrons and holes [32].

3.3. Optical properties

The absorption spectra of the synthesized materials are shown in Fig. 7 and, as can be observed, P-doped C_3N_4 material exhibits an absorption profile similar to the pristine C_3N_4, whereas the inclusion of antimony results in a notable enhancement of the absorption band, peaking at approximately 380 nm, and an extension of the absorption range into the visible region, reaching up to 550 nm, as perceived in Fig. 7 (right).

From the study in diffuse reflectance, processing the Kubelka-Munk function of the spectra, through the Tauc plot method [48] it is possible to determine the optical band gaps of the materials (Table 1), highlighting that the introduction of phosphorous and antimony led to narrowed band gaps and consequently to an increase in visible light harvesting.

The Mott-Schottky plots in Fig. 8 indicate a progressive increase in the conduction band minimum of the prepared samples, transitioning from -1.26 eV for the pristine C_3N_4 to -0.62 eV for Sb5 P-doped C_3N_4. Using this information, together with the energy band gaps obtained by Tauc plots, the band position diagram was assessed for pristine C_3N_4 and modified samples, as depicted in Fig. 9.

The phosphorous doping and Sb introduction appear to be pivotal in shifting the upper limit of the valence band toward more positive values. Considering the purpose of these photocatalysts, one must remember

Table 1
Band gap (eV) values determined from absorption spectra for different synthesized materials.

Sample	Band gap (eV)
M-C_3N_4	2.75
P-doped M-C_3N_4	2.72
Sb0.5 P-doped M-C_3N_4	2.65
Sb1 P-doped M-C_3N_4	2.63
Sb3 P-doped M-C_3N_4	2.57
Sb5 P-doped M-C_3N_4	2.55

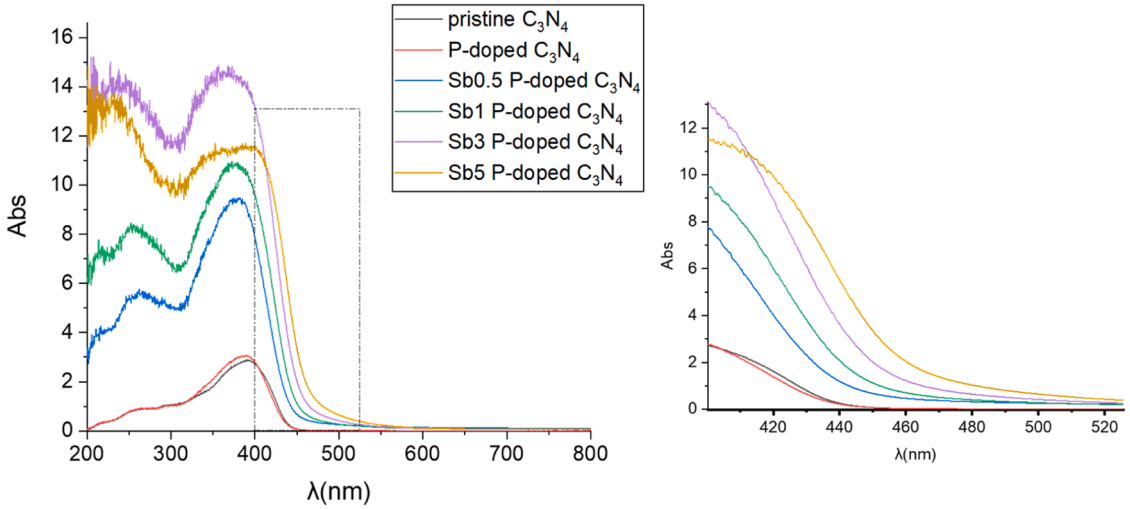

Fig. 7. DR-UV–Vis spectra for the obtained materials (left) and enlargement of the 400–525 nm region (right).

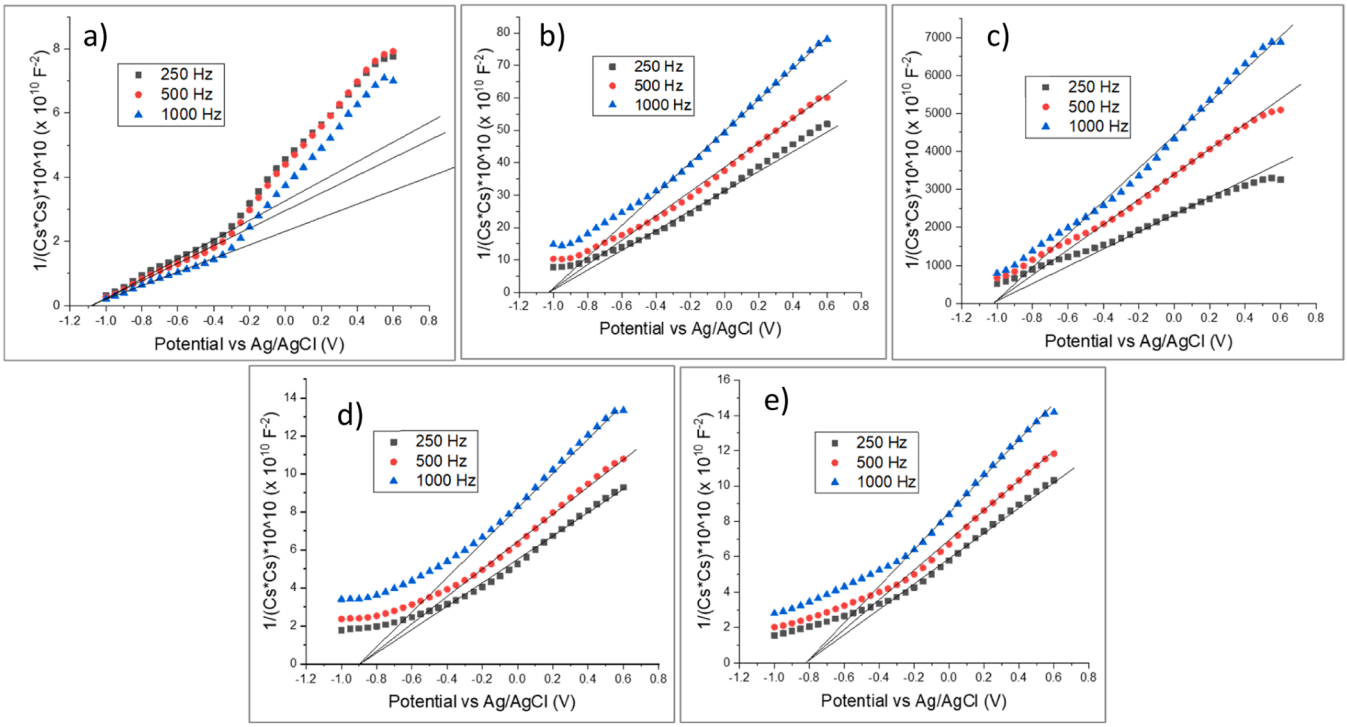

Fig. 8. Mott-Schottky curves of the modified materials: a) pristine C_3N_4, b) P-doped C_3N_4, c) Sb0.5 P-doped C_3N_4, d) Sb1 P-doped C_3N_4 e) Sb5 P-doped C_3N_4.

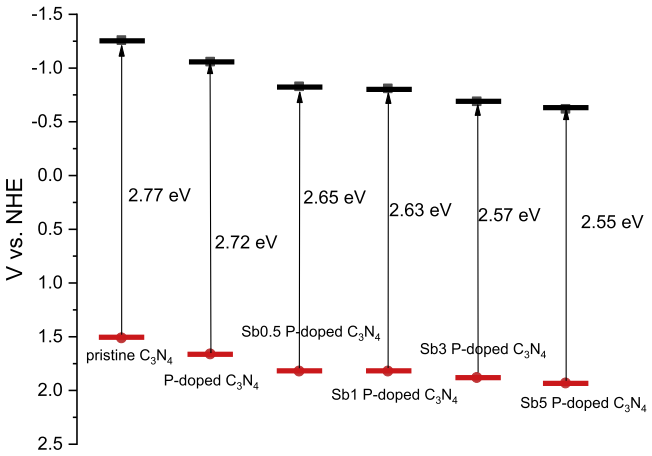

Fig. 9. Derived band position diagram.

that in order to enhance the overall efficiency of producing hydrogen peroxide, it is essential to promote either the two-electron oxygen reduction reaction (ORR) and having a sufficient oxidization potential for overcoming the large overpotential of water oxidation [40]. Therefore, the increase in valence band potential values makes it more plausible that water oxidation may occur on these catalysts, thus enabling effective H_2O_2 production from O_2 and water.

3.4. Hydrogen peroxide production

The photoactivity of the synthesized photocatalysts was evaluated for hydrogen peroxide production without adding a sacrificial agent, hence Milli-Q water was used as reaction medium, and oxygen was bubbled for 15 min before irradiation. As shown in Fig. 10a, the use of pristine carbon nitride led to a poor production of H_2O_2, whereas the doping with phosphorus and antimony allowed to significantly increase the concentration produced.

The optimal quantity of Sb was determined to be 1 mmol, resulting in the generation of 3 mg/L after a five-hour period. This amount is over seven times greater than what is produced by the unmodified carbon nitride. The capability to produce H_2O_2 is slightly decreased after the third cycle of catalyst reuse (see Fig. S2).

As the ultimate objective is to use photocatalysts in conditions closely resembling those found in practical treatment systems, experiments were replicated without oxygen bubbling. Despite this, an efficient production of H_2O_2 was maintained, with values that, after five hours were only slightly lower than those obtained when oxygen was introduced, as illustrated in Fig. 10c. The increased H_2O_2 production for the co-doped C_3N_4 under these conditions is supported by the results obtained via EPR measurements. In Figure S1 the integrated area of EPR signal directly correlated to the ·OH radicals concentration measured for pristine material and P doped or co-doped samples. Despite a similar yield of OH radicals produced, P-doped as well as the bare C_3N_4 sample show the highest activity in the formation of ·OH radicals in the first minutes, while the Sb1 P-doped C_3N_4 activates a little bit later but then maintains the activity much longer than the other samples. However, there was a slightly reduced increasing trend, as highlighted in Fig. 10b. In fact, after three hours, the production reached a plateau, and this can be explained by considering that at first instance the generation of hydrogen peroxide can occur through the oxygen reduction reaction (ORR). Once the oxygen in the reaction vessel is depleted, the production yield decreases, since more oxygen needs to be produced by water oxidation and at the same time, the competitive decomposition of the produced hydrogen peroxide can take place.

The discussed results refer to the experiments performed using visible light, then they were repeated including the near UV-A (λ>340 nm) and obtained data are shown in Fig. 11.

In this case, it is evident that the overall production of hydrogen peroxide improves, especially by increasing the amount of antimony in the synthesis step, but the linear trend of increasing production with time is completely lost; in fact, after two hours the H_2O_2 concentration drops, returning to values like those obtained after one hour of irradiation.

This phenomenon could be explained considering the recombination

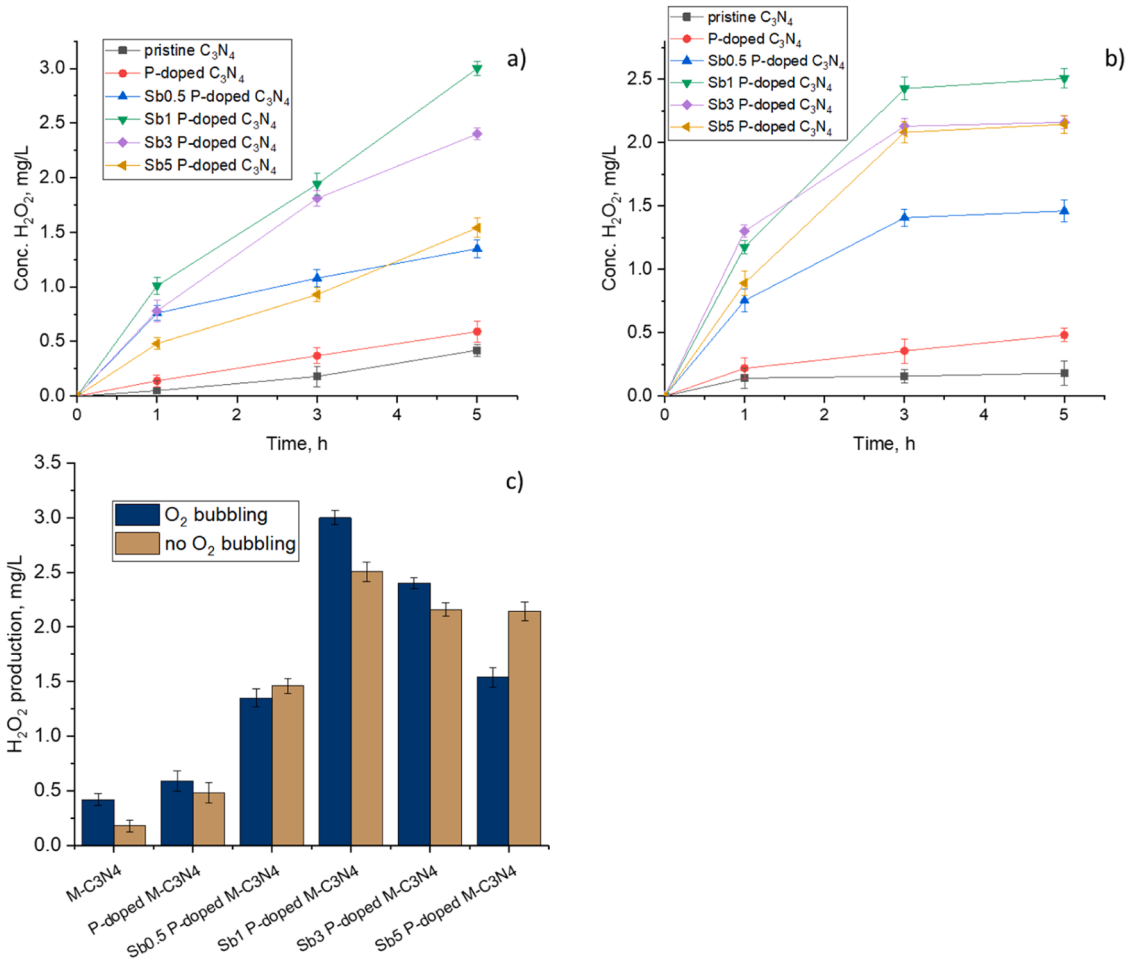

Fig. 10. Hydrogen peroxide production over 5 h of reaction under visible light irradiation (420<λ<800 nm) with (a), without (b) 15 min of oxygen bubbling and comparison after 5 h (c).

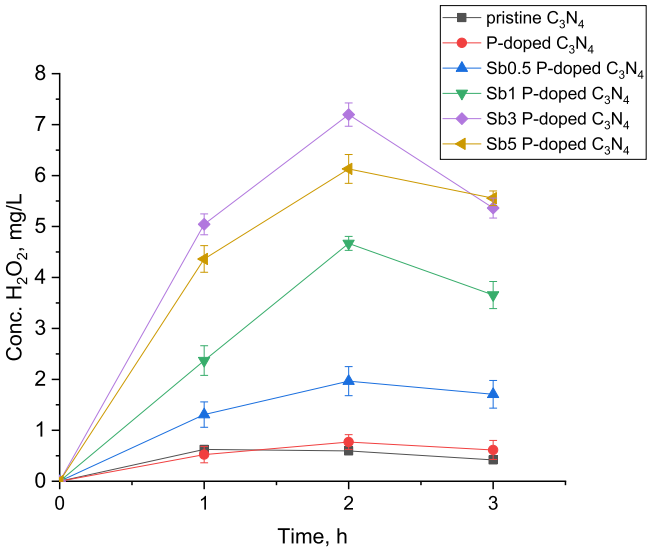

Fig. 11. Hydrogen peroxide production over 3 h of reaction under UV–vis light irradiation (340<λ<800 nm) without oxygen bubbling.

with the holes resulting in the decomposition to water or it can be due to the release of Na^+ ions in solution. In fact, from EDS analyses the presence of sodium in the prepared materials containing antimony, was highlighted; ICP-OES analyses of the solutions after irradiation and filtration of the photocatalyst were performed, showing a considerable release of Na into solution, amounting to 10 ppm after 3 h for the sample obtained using Sb1 P-doped C_3N_4 and with increasing concentrations over time and using the materials with higher Sb content.

3.5. *Organic substrates degradation*

The newly developed materials underwent testing not only for hydrogen peroxide production but also for the photocatalytic degradation of organic substances. Carbamazepine was chosen as a target pollutant, and its degradation efficiency was assessed by irradiating the solution containing the drug and the photocatalyst suspension with a Xenon lamp equipped with cut-offs to select wavelengths greater than 340 or 420 nm. In dark conditions, adsorption tests revealed that no adsorption occurred during the sixteen-hour period considered.

It is worth noting that when irradiation was conducted using a filter that entirely excluded UV-A radiation (as depicted in Fig. 12a), the degradation of carbamazepine was notably poor. However, when the wavelength range was expanded (as shown in Fig. 12b), complete degradation of the substrate occurred within 4 h for the most effective materials. In this scenario, contrary to what was observed in peroxide production, the most efficient photocatalysts were those not containing antimony, namely the pristine carbon nitride and the phosphorus-doped one, indicating an opposite trend. This divergence can be elucidated by recognizing that the primary mechanism for carbamazepine degradation predominantly involves photogenerated holes, as validated by

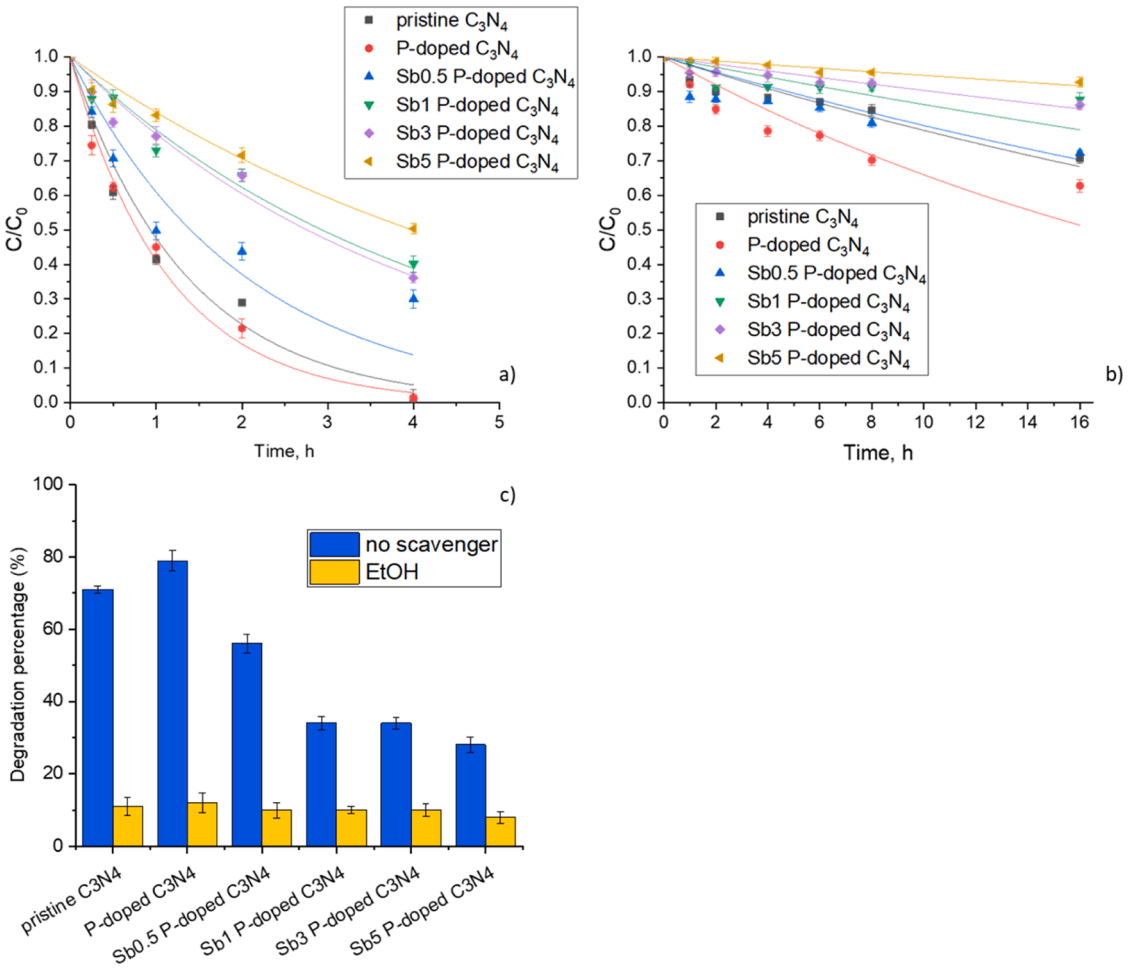

Fig. 12. Carbamazepine degradation over time using λ>420 nm (a) or λ>340 nm irradiation (b) and degradation percentage after 2 h of irradiation (λ>340 nm) with and without the holes scavenger (c).

experiments conducted in the presence of a hole scavenger like ethanol (as illustrated in Fig. 12c). In fact, the degradation rate of carbamazepine in such cases was significantly lower compared to when no scavenger was present. For this reason, the materials that are most efficient in producing hydrogen peroxide by oxygen reduction and water oxidation, on the other hand, are the least efficient for the degradation of a substrate like carbamazepine.

Moreover, considering the band diagram results presented in Fig. 9, pristine C_3N_4 and P-doped C_3N_4 exhibit an advantage in terms of oxidizing capability. However, these two materials have minimal capacity for generating H_2O_2, indicating that the primary reaction involves the production of superoxide anion radicals through a one-electron reduction of oxygen. In this context, pristine C_3N_4, which possesses a more negatively positioned CB, enjoys a favourable position due to these trade-offs, resulting in a good reaction trend.

As for Sbx P-doped C_3N_4, with an increasing quantity of Sb, the VB shifts towards a more positive position, consequently enhancing its oxidizing potential. Conversely, the CB also shifts towards the positive side, diminishing its capacity to generate hydrogen peroxide and superoxide anion radicals through one-electron reduction of oxygen. Once again, a reaction trend resulting from these trade-offs was evident.

4. Conclusions

The present study aimed to create atomically dispersed antimony P-doped carbon nitride with the objective of generating hydrogen peroxide under visible light irradiation and facilitating the degradation of organic pollutants. Photocatalysts were prepared via facile syntheses and comprehensive characterization techniques were employed to assess materials features. The P-doping and introduction of antimony were confirmed by FE-SEM, EDS and XPS analyses and resulted in enhanced visible light absorption, a reduction in the band gap energy, and a shift of the valence band edge to a less positive position and reduced charge recombination. Photocatalysts performance was evaluated in terms of hydrogen peroxide production and the degradation of carbamazepine. Pristine C_3N_4 exhibited limited hydrogen peroxide production, but the introduced modifications led to an increased yield, showing an upward trend over time. The optimal amount of antimony was determined to be 1 mmol, resulting in more than a sevenfold increase in hydrogen peroxide production compared to pristine carbon nitride. Considering carbamazepine degradation, expanding the light spectrum to include near-UV radiation, pollutant removal was achieved within a few hours. The efficacy of the synthesized materials in hydrogen peroxide production suggests potential future applications, such as utilizing atomically dispersed antimony P-doped carbon nitride photocatalysts in Fenton-like processes or incorporating peroxidase enzymes to enhance degradative performance.

Funding

This research was funded by funding from the European Union's Horizon 2020 Research and Innovation Programme under the MarieSkłodowska-Curie Grant Agreement No101007578 (SusWater).

Data availability

Data, associated metadata, and calculation tools are available from the corresponding author.

CRediT authorship contribution statement

Elisa Gaggero: Data curation, Investigation, Writing – original draft, Writing – review & editing. **Wenan Cai:** Data curation, Writing – review & editing. **Paola Calza:** Funding acquisition, Writing – review & editing. **Teruhisa Ohno:** Conceptualization, Supervision, Writing – review & editing, Resources.

Declaration of competing interest

The authors declare that they have no known competing financial interests or personal relationships that could have appeared to influence the work reported in this paper.

Supplementary materials

Supplementary material associated with this article can be found, in the online version, at doi:10.1016/j.surfin.2024.104143.

References

[1] E. Lopez-Gunn, M. Ramón Llamas, *Re*-thinking water scarcity: can science and technology solve the global water crisis? Nat. Resour. Forum 32 (2008) 228–238.

[2] J. Liu, H. Yang, S.N. Gosling, M. Kummu, M. Flörke, S. Pfister, N. Hanasaki, Y. Wada, X. Zhang, C. Zheng, J. Alcamo, T. Oki, Water scarcity assessments in the past, present, and future, Earth Future 5 (2017) 545–559.

[3] M.E. Borges, M. Sierra, E. Cuevas, R.D. García, P. Esparza, Photocatalysis with solar energy: sunlight-responsive photocatalyst based on TiO2 loaded on a natural material for wastewater treatment, Sol. Energy 135 (2016) 527–535.

[4] K.K. Parul, R. Badru, P.P. Singh, S. Kaushal, Photodegradation of organic pollutants using heterojunctions: a review, J. Environ. Chem. Eng. 8 (2020) 103666.

[5] M.R.D. Khaki, M.S. Shafeeyan, A.A.A. Raman, W.M.A.W. Daud, Application of doped photocatalysts for organic pollutant degradation - a review, J. Environ. Manag. 198 (2017) 78–94.

[6] Q. You, C. Zhang, M. Cao, B. Wang, J. Huang, Y. Wang, S. Deng, G. Yu, Defects controlling, elements doping, and crystallinity improving triple-strategy modified carbon nitride for efficient photocatalytic diclofenac degradation and H_2O_2 production, Appl. Catal. B Environ. 321 (2023).

[7] L. Zhou, W. Song, Z. Chen, G. Yin, Degradation of organic pollutants in wastewater by bicarbonate-activated hydrogen peroxide with a supported cobalt catalyst, Environ. Sci. Technol. 47 (2013) 3833–3839.

[8] J. Xie, J. Jing, J. Gu, J. Guo, Y. Li, M. Zhou, Hydrogen peroxide generation from gas diffusion electrode for electrochemical degradation of organic pollutants in water: a review, J. Environ. Chem. Eng. 10 (2022) 107882.

[9] A.M. Azevedo, V.C. Martins, D.M. Prazeres, V. Vojinovic, J.M. Cabral, L.P.J.B.A.R. Fonseca, Horseradish peroxidase: a valuable tool in biotechnology, 9 (2003) 1387–2656.

[10] M. Sarro, N.P. Gule, E. Laurenti, R. Gamberini, M.C. Paganini, P.E. Mallon, P. Calza, ZnO-based materials and enzymes hybrid systems as highly efficient catalysts for recalcitrant pollutants abatement, Chem. Eng. J. 334 (2018) 2530–2538.

[11] M. Bilal, T. Rasheed, Y. Zhao, H.M.J.I.J.O.B.M. Iqbal, Agarose-chitosan hydrogel-immobilized horseradish peroxidase with sustainable bio-catalytic and dye degradation properties, 124 (2019) 742–749.

[12] C. Zhang, X.J.C.I. Cai, Immobilization of horseradish peroxidase on Fe3O4/ nanotubes composites for biocatalysis-degradation of phenol, 26 (2019) 379–396.

[13] Z. Teng, W. Cai, W. Sim, Q. Zhang, C. Wang, C. Su, T. Ohno, Photoexcited single metal atom catalysts for heterogeneous photocatalytic H_2O_2 production: pragmatic guidelines for predicting charge separation, Appl. Catal. B Environ. 282 (2021).

[14] J.M. Campos-Martin, G. Blanco-Brieva, J.L.G. Fierro, Hydrogen peroxide synthesis: an outlook beyond the anthraquinone process, Angew. Chem. Int. Ed. 45 (2006) 6962–6984.

[15] L. Zhou, J. Lei, F. Wang, L. Wang, M.R. Hoffmann, Y. Liu, S.I. In, J. Zhang, Carbon nitride nanotubes with in situ grafted hydroxyl groups for highly efficient spontaneous H_2O_2 production, Appl. Catal. B Environ. 288 (2021) 119993.

[16] S. Li, G. Dong, R. Hailili, L. Yang, Y. Li, F. Wang, Y. Zeng, C. Wang, Effective photocatalytic H_2O_2 production under visible light irradiation at g-C_3N_4 modulated by carbon vacancies, Appl. Catal. B Environ. 190 (2016) 26–35.

[17] W.J. Ong, L.L. Tan, Y.H. Ng, S.T. Yong, SP.J.C.R. Chai, Graphitic carbon nitride (g-C3N4)-based photocatalysts for artificial photosynthesis and environmental remediation: are we a step closer to achieving sustainability?, 116 (2016) 7159–7329.

[18] Y. Shiraishi, S. Kanazawa, Y. Sugano, D. Tsukamoto, H. Sakamoto, S. Ichikawa, T.J. A.C. Hirai, Highly selective production of hydrogen peroxide on graphitic carbon nitride (g-C3N4) photocatalyst activated by visible light, 4 (2014) 774–780.

[19] F.K. Kessler, Y. Zheng, D. Schwarz, C. Merschjann, W. Schnick, X. Wang, M.J.J.N.R. M. Bojdys, Functional carbon nitride materials—design strategies for electrochemical devices, 2 (2017) 1–17.

[20] Z. Teng, W. Cai, T. Ohno, Functionalized graphitic carbon nitrides for photocatalytic H_2O_2 production: desired properties leading to rational catalyst design, KONA Powder Part. J. 40 (2023) 124–148.

[21] X. Chen, J. Zhang, X. Fu, M. Antonietti, X. Wang, Fe-g-C_3N_4-catalyzed oxidation of benzene to phenol using hydrogen peroxide and visible light, J. Am. Chem. Soc. 131 (2009) 11658–11659.

[22] S. Hu, F. Li, Z. Fan, F. Wang, Y. Zhao, Z. Lv, Band gap-tunable potassium doped graphitic carbon nitride with enhanced mineralization ability, Dalton Trans. 44 (2015) 1084–1092.

[23] S. Hu, X. Chen, Q. Li, F. Li, Z. Fan, H. Wang, Y. Wang, B. Zheng, G. Wu, Fe^{3+} doping promoted N_2 photofixation ability of honeycombed graphitic carbon nitride: the experimental and density functional theory simulation analysis, Appl. Catal. B Environ. 201 (2017) 58–69.

[24] S. Hu, X. Qu, P. Li, F. Wang, Q. Li, L. Song, Y. Zhao, X. Kang, Photocatalytic oxygen reduction to hydrogen peroxide over copper doped graphitic carbon nitride hollow microsphere: the effect of Cu(I)-N active sites, Chem. Eng. J. 334 (2018) 410–418.

[25] S.C. Yan, Z.S. Li, Z.G. Zou, Photodegradation of rhodamine B and methyl orange over boron-doped g-C_3N_4 under visible light irradiation, Langmuir 26 (2010) 3894–3901.

[26] G. Liu, P. Niu, C. Sun, S.C. Smith, Z. Chen, G.Q. Lu, H.M. Cheng, Unique electronic structure induced high photoreactivity of sulfur-doped graphitic C_3N_4, J. Am. Chem. Soc. 132 (2010) 11642–11648.

[27] M. Bellardita, E.I. García-López, G. Marcì, I. Krivtsov, J.R. García, L. Palmisano, Selective photocatalytic oxidation of aromatic alcohols in water by using P-doped g-C_3N_4, Appl. Catal. B Environ. 220 (2018) 222–233.

[28] K. Jinguji, M. Watanabe, R. Morita, Y. Takaoka, M.S. Hossain, J.T. Song, A. Takagaki, J. Matsuda, T. Ishihara, Visible light driven hydrogen peroxide production by oxygen and phosphorus co-doped CoP-C_3N_4 photocatalyst, Catal. Today 426 (2024).

[29] G. Yu, K. Gong, C. Xing, L. Hu, H. Huang, L. Gao, D. Wang, X. Li, Dual P-doped-site modified porous g-C_3N_4 achieves high dissociation and mobility efficiency for photocatalytic H_2O_2 production, Chem. Eng. J. 461 (2023).

[30] S. Hu, L. Ma, J. You, F. Li, Z. Fan, G. Lu, D. Liu, J. Gui, Enhanced visible light photocatalytic performance of g-C3N4 photocatalysts co-doped with iron and phosphorus, Appl. Surf. Sci. 311 (2014) 164–171.

[31] X. Dang, R. Yang, Z. Wang, S. Wu, H. Zhao, Efficient visible-light activation of molecular oxygen to produce hydrogen peroxide using P doped g-C_3N_4 hollow spheres, J. Mater. Chem. A 8 (2020) 22720–22727.

[32] A. Hussain, N. Ali, S. Ali, J. Hou, I. Aslam, H. Naeem, M. Boota, M. Ul-Hussan, J. Yin, X.J.R.O.C.I. Wang, Diverse morphological study for nonmetal-doped g-C3N4 composites with narrow bandgap for improved photocatalytic activity, Res. Chem. Internediates 48 (2022) 2857–2870.

[33] Z. Teng, Q. Zhang, H. Yang, K. Kato, W. Yang, Y.R. Lu, S. Liu, C. Wang, A. Yamakata, C. Su, B. Liu, T. Ohno, Atomically dispersed antimony on carbon nitride for the artificial photosynthesis of hydrogen peroxide, Nat. Catal. 4 (2021) 374–384.

[34] L. Zhang, Z. Jin, J. Huang, Y. Zhang, S. Huang, Z. Wang, Y.J. Zeng, V. Malgras, S. Ruan, Y. Yamauchi, Carbon nitride functionalized with Sb resulting in high photocatalytic activity, ACS Appl. Energy Mater. 4 (2021) 5677–5686.

[35] S. Feijoo, M. Kamali, R. Dewil, A review of wastewater treatment technologies for the degradation of pharmaceutically active compounds: carbamazepine as a case study, Chem. Eng. J. 455 (2023).

[36] Y. Zhang, S.U. Geißen, Prediction of carbamazepine in sewage treatment plant effluents and its implications for control strategies of pharmaceutical aquatic contamination, Chemosphere 80 (2010) 1345–1352.

[37] C. Tixier, H.P. Singer, S. Oellers, S.R.J.E.S. Müller, Technology, occurrence and fate of carbamazepine, clofibric acid, diclofenac, ibuprofen, ketoprofen, and naproxen in surface waters, 37 (2003) 1061–1068.

[38] J.E. Frew, P. Jones, G. Scholes, Spectrophotometric determination of hydrogen peroxide and organic hydroperoxides at low concentrations in aqueous solution, Anal. Chim. Acta 155 (1983) 139–150.

[39] F. Fina, S.K. Callear, G.M. Carins, J.T.S. Irvine, Structural investigation of graphitic carbon nitride via XRD and neutron diffraction, Chem. Mater. 27 (2015) 2612–2618.

[40] Z. Teng, W. Cai, S. Liu, C. Wang, Q. Zhang, S. Chenliang, T. Ohno, Bandgap engineering of polymetric carbon nitride copolymerized by 2,5,8-triamino-tri-s-triazine (melem) and barbituric acid for efficient nonsacrificial photocatalytic H_2O_2 production, Appl. Catal. B Environ. 271 (2020).

[41] S. Hu, L. Ma, J. You, F. Li, Z. Fan, F. Wang, D. Liu, J. Gui, A simple and efficient method to prepare a phosphorus modified g-C_3N_4 visible light photocatalyst, RSC Adv. 4 (2014) 21657–21663.

[42] Y. Zhou, L. Zhang, J. Liu, X. Fan, B. Wang, M. Wang, W. Ren, J. Wang, M. Li, J. Shi, Brand new P-doped g-C_3N_4: enhanced photocatalytic activity for H_2 evolution and Rhodamine B degradation under visible light, J. Mater. Chem. A 3 (2015) 3862–3867.

[43] S. Guo, Y. Tang, Y. Xie, C. Tian, Q. Feng, W. Zhou, B. Jiang, P-doped tubular g-C_3N_4 with surface carbon defects: universal synthesis and enhanced visible-light photocatalytic hydrogen production, Appl. Catal. B Environ. 218 (2017) 664–671.

[44] S. Liu, H. Zhu, W. Yao, K. Chen, D. Chen, One step synthesis of P-doped g-C_3N_4 with the enhanced visible light photocatalytic activity, Appl. Surf. Sci. 430 (2018) 309–315.
[45] N. He, S. Cao, J. Gu, A. Uddin, C. Zhang, Y. Yu, H. Chen, F. Jiang, Well-designed oxidized Sb/g-C(3)N(4) 2D/2D nanosheets heterojunction with enhanced visible-light photocatalytic disinfection activity, J. Colloid Interface Sci. 606 (2022) 1284–1298.
[46] M. Anpo, M. Che, Applications of photoluminescence techniques to the characterization of solid surfaces in relation to adsorption, catalysis, and photocatalysis, 1999, pp. 119–257.
[47] S.A. Empedocles, R. Neuhauser, K. Shimizu, M.G. Bawendi, Photoluminescence from single semiconductor nanostructures, Adv. Mater. 11 (1999) 1243–1256.
[48] P. Makula, M. Pacia, W. Macyk, How to correctly determine the band gap energy of modified semiconductor photocatalysts based on UV–Vis spectra, J. Phys. Chem. Lett. 9 (2018) 6814–6817.